

INFLUENCE OF NUCLEAR REACTION RATE UNCERTAINTIES ON NEUTRON STAR PROPERTIES EXTRACTED FROM X-RAY BURST MODEL-OBSERVATION COMPARISONS

ZACH MEISEL, GRANT MERZ, AND SOPHIA MEDVID

Institute of Nuclear & Particle Physics, Department of Physics & Astronomy, Ohio University, Athens, Ohio 45701, USA

Draft version, December 19, 2018

ABSTRACT

Type-I X-ray bursts can be used to determine properties of accreting neutron stars via comparisons between model calculations and astronomical observations, exploiting the sensitivity of models to astrophysical conditions. However, the sensitivity of models to nuclear physics uncertainties calls into question the fidelity of constraints derived in this way. Using X-ray burst model calculations performed with the code MESA, we investigate the impact of uncertainties for nuclear reaction rates previously identified as influential and compare them to the impact of changes in astrophysical conditions, using the conditions that are thought to best reproduce the source GS 1826-24 as a baseline. We find that reaction rate uncertainties are unlikely to significantly change conclusions about the properties of accretion onto the neutron star surface for this source. However, we find that reaction rate uncertainties significantly hinder the possibility of extracting the neutron star mass-radius ratio by matching the modeled and observed light curves due to the influence of reaction rates on the modeled light curve shape. Particularly influential nuclear reaction rates are $^{15}\text{O}(\alpha, \gamma)$ and $^{23}\text{Al}(p, \gamma)$, though other notable impacts arise from $^{14}\text{O}(\alpha, p)$, $^{18}\text{Ne}(\alpha, p)$, $^{22}\text{Mg}(\alpha, p)$, $^{24}\text{Mg}(\alpha, \gamma)$, $^{59}\text{Cu}(p, \gamma)$, and $^{61}\text{Ga}(p, \gamma)$. Furthermore, we find that varying some nuclear reaction rates within their uncertainties has an impact on the neutron star crust composition and thermal structure that is comparable to relatively significant changes accretion conditions.

1. INTRODUCTION

Thermonuclear explosions powered by hydrogen and helium burning on the surfaces of accreting neutron stars, known as Type-I X-ray bursts, have been the subject of modeling efforts since even before they were first observed (Meisel et al. 2018). Early efforts established a sensitivity of model calculation results to underlying neutron star properties, such as the mass and radius, and the details of accretion rate and accreted composition (Fujimoto et al. 1981; Ayasli & Joss 1982). It has also been understood since the beginning that the thermonuclear origin of the bursts lends model calculations to a sensitivity to the nuclear physics input (Joss 1977; Wallace & Woosley 1981). An outstanding question is to what extent the sensitivity of model results to nuclear physics uncertainties limits the ability of model-observation comparisons to extract constraints on astrophysical conditions by exploiting the sensitivity of model results to these conditions.

In the past decade several works have undertaken model-observation comparisons to constrain the astrophysical conditions for specific X-ray bursting sources. This has been enabled by the construction of catalogues containing particularly well-characterized sources that make for good modeling targets, e.g. Galloway et al. (2008, 2017). Examples include constraints for the accretion properties of SAX J1808.4-3658 (Johnston et al. 2018) and accretion-based heating for an object like EXO 0748-676 (Keek & Heger 2017).

The most common target for model-observation comparisons has been GS 1826-24, selected for its textbook bursting behavior (Bildsten 2000; Galloway et al. 2008). Galloway et al. (2004) used a simple ignition model to

constrain the accretion metallicity for this source by matching the trend in the burst recurrence time for increasing accretion rate. Heger et al. (2007) constrained the accretion rate and metallicity by matching the shape of the observed light curve for one bursting epoch to results from KEPLER (Weaver et al. 1978; Woosley et al. 2004) model calculations performed with an assumed neutron star mass and radius, which Galloway et al. (2017) repeated for updated observational data. Zambir et al. (2012) employed the best-fit model from Heger et al. (2007) to constrain the neutron star compactness by a matching the observed light curve flux and, for a separate constraint, the light curve shape. Meisel (2018) used MESA (Paxton et al. 2011, 2013, 2015, 2018) to perform a simultaneous matching of the recurrence time and light curve shape for multiple bursting epochs using a grid of simulated astrophysical conditions to simultaneously constrain the accretion rate and composition, accretion-based heating, and neutron star compactness. Note that each of the aforementioned studies adopted a single set of nuclear physics input, though calculation results are known to be sensitive to nuclear physics input.

Parikh et al. (2008) and Parikh et al. (2009) employed post-processing calculations to demonstrate the sensitivity of X-ray burst nucleosynthesis to nuclear reaction rates and masses, respectively. More recently, single-zone (i.e. zero-dimensional) models with self-consistent temperature and density evolution have explored the impact of uncertainties in nuclear reaction rates and nuclear masses on X-ray burst light curves (Cyburt et al. 2016; Schatz & Ong 2017). Cyburt et al. (2016) also employed multizone (i.e. one-dimensional) calculations with KEPLER to follow-up on reaction rates that were identified as important in the single-zone calculations. Note that the impact on the burst light curve has been described

in these works either using visual comparisons or an integral of the absolute difference between the light curves of two models.

To date, it has not been directly explored how nuclear physics uncertainties influence astrophysical constraints derived from model-observation comparisons for a specific source. We investigate this in the present work, employing the model calculations described in Meisel (2018) and focusing on conditions similar to those required to reproduce the observed features of GS 1826-24. This is presented as follows. Section 2 discusses the production of model light curves. Section 3 describes the nuclear reaction rates for which the model sensitivity is being assessed. Section 4 examines the influence of varying these reaction rates within their present uncertainties on model light curve properties, while Section 5 investigates the influence on model nucleosynthesis. Section 6 details the method for matching the shape of a modeled light curve to observational data to extract a mass-radius ratio and demonstrates the strong sensitivity of these results to certain nuclear physics uncertainties. Section 7 concludes with a summary of our findings.

2. MODEL CALCULATIONS

The model calculations used in this work are the same as in Meisel (2018). The pertinent details are recapitulated here for convenience.

2.1. Code Details and Microphysics

The code MESA version 9793 was used to calculate the X-ray luminosity over time and burst ashes produced by nuclear burning in ~ 1000 zones constructed to resemble an accreting neutron star envelope. Corrections include a post-Newtonian modification of the local gravity for general relativistic effects and a time-dependent mixing length theory (Heney et al. 1965; Paxton et al. 2011) for convection. The time resolution and spatial resolution adapt according to the MESA controls `varcontrol_target=1d-3` and `mesh_delta_coeff=1.0` (Paxton et al. 2013). The ~ 0.01 km thick envelope has an inner boundary of neutron star mass $M_{\text{NS}} = 1.4 M_{\odot}$ and radius $R_{\text{NS}} = 11.2$ km. The 304 isotope network of Fisker et al. (2008) was used with REACLIB (Cyburt et al. 2010) version 2.2 as the baseline nuclear reaction rate library. The solar metal fraction of Grevesse & Sauval (1998) was used to distribute the accreted metals.

Astrophysical conditions which were varied between different model calculations include the accretion rate \dot{M} , metallicity of the accreted composition Z , accretion-based heating at the base of the envelope Q_b , and hydrogen mass fraction $X(H)$. The helium mass fraction Y was adjusted to enforce $X(H) + Y + Z = 1$. $\dot{M} = 0.05, 0.07, 0.08, 0.11, 0.15, 0.17 \dot{M}_{\text{E}}$, where $\dot{M}_{\text{E}} = 1.75 \times 10^{-8} M_{\odot}/\text{yr}$ is the Eddington accretion rate (Schatz et al. 1999), were explored to sample \dot{M} for the observed GS 1826-24 epochs from 1998, 2000, and 2007 (Galloway et al. 2008) and the observed \dot{M} scaled up by ~ 2 (Meisel 2018). $Z = 0.01, 0.02$ were used to investigate the solar Z favored by previous investigations of GS 1826-24 (Galloway et al. 2004; Heger et al. 2007) and a slight reduction from that value. $Q_b = 0.1, 0.5, 1.0$ MeV/u were chosen to mimic shallow heating thought to occur in the outer

layers of accreting neutron stars, with the lower-bound roughly corresponding to heat from electron-captures induced by accretion (Gupta et al. 2007; Meisel et al. 2016) and the upper bound corresponding to a typical amount of heating inferred from model-observation comparisons of neutron star crust cooling (Turlione et al. 2015). While larger Q_b have been inferred (Deibel et al. 2015), we did not explore these since this can lead to short waiting-time bursts (Keek & Heger 2017), which GS 1826-24 does not exhibit. In MESA base heating is achieved by fixing the luminosity of the base of the envelope, so that the base luminosity depended on Q_b and \dot{M} of the model. $X(H) = 0.50, 0.55, 0.60, 0.65, 0.70, 0.75$ were investigated to sample a range of conditions from hydrogen-poor to hydrogen-rich while still maintaining a sufficient amount of hydrogen to avoid pure helium bursts.

2.2. Light Curve Construction

To mitigate the numerical noise that leads to some burst-to-burst variability and occasional sharp features in an individual burst light curve, MESA light curves for a sequence of bursts calculated with one set of astrophysical conditions were combined to an average light curve, as is frequently done with observational data. The first burst in a sequence was excluded, since the lack of ashes from prior bursts leads to an atypically energetic burst (Woosley et al. 2004). Bursts in a sequence were mapped onto a uniform time grid with a linear spline, smoothed by averaging the luminosity over a ± 1 s time window, and aligned in time by defining a luminosity threshold being crossed at time $t = 0$. The light curves corresponding to a sequence (typically 10 – 20 bursts) were combined to achieve an average light curve and an uncertainty band, where fewer bursts in a sequence will generally result in a larger band. See Meisel (2018) for an example of this process.

3. NUCLEAR REACTION RATES VARIED

Nuclear reaction rates were varied for calculations employing the astrophysical conditions recently found to best reproduce light curve features of GS 1826-24 (Meisel 2018): $\dot{M} = 0.17 \dot{M}_{\text{E}}$, $Z = 0.02$, $Q_b = 0.1$ MeV/u, $X(H) = 0.70$. Due to computational expense, the set of reaction rates under investigation was limited to the 19 rate variations found to have a significant impact on X-ray burst light curves calculated with KEPLER for similar astrophysical conditions (Cyburt et al. 2016). Rate variation factors of 10 and 100 were adopted for reactions proceeding through high and low level density regions in the compound nucleus, respectively, following the approach of Cyburt et al. (2016). The sources for other rate variation factors are discussed below. We note that the rate variation factors should be considered plausible but somewhat generous nuclear physics uncertainties, where the intention is that more rigorous uncertainty evaluations could be pursued for reactions found to be influential.

Detailed discussions of nuclear reactions relevant for X-ray bursts can be found in van Wormer et al. (1994); Wiescher et al. (1999); Woosley et al. (2004); Fisker et al. (2004, 2008); Cyburt et al. (2016); Meisel et al. (2018). The role of the rates varied in this work are briefly discussed here in order to help understand their potential

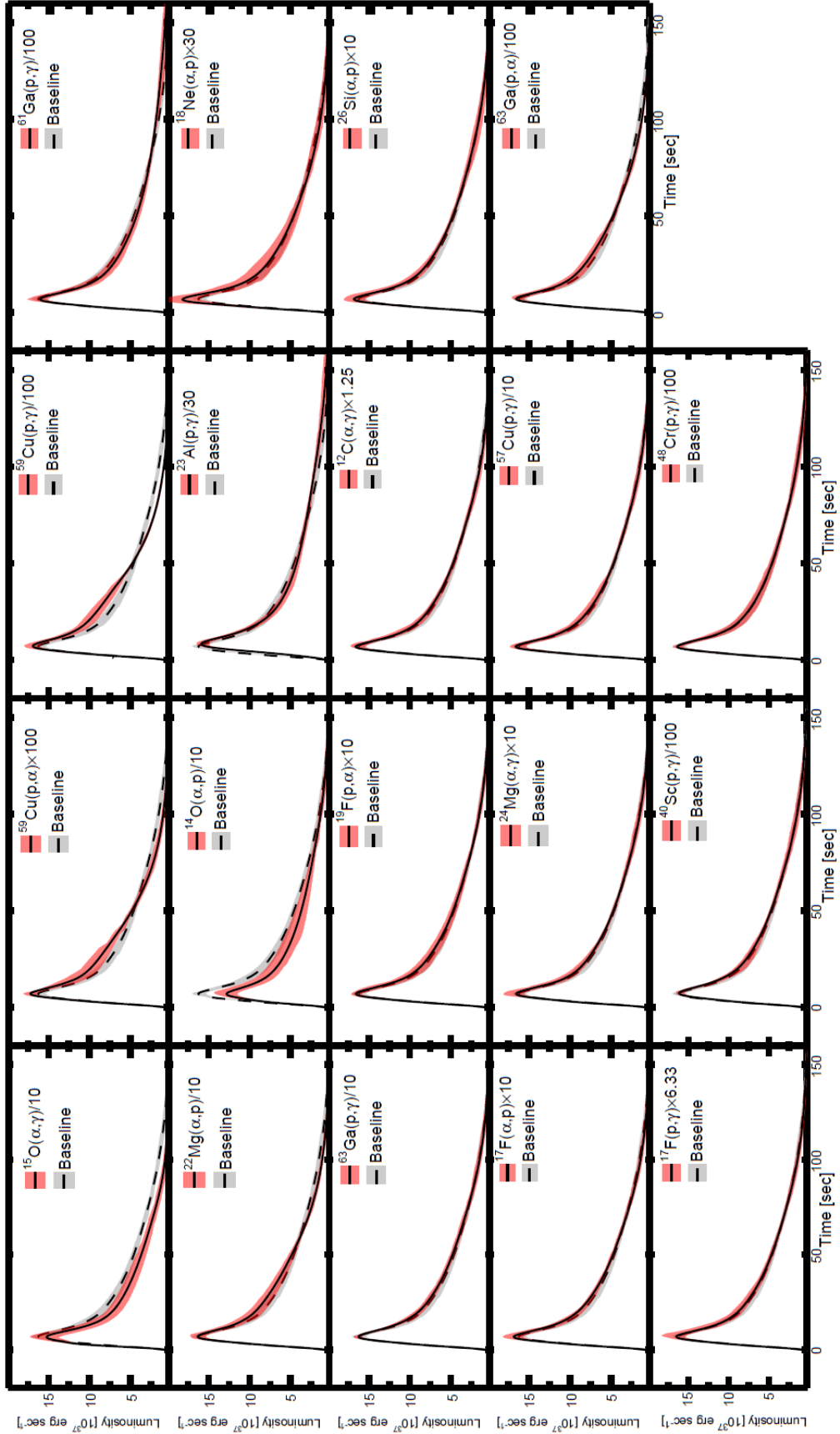


FIG. 1.— Light curves calculated using a varied reaction rate (red band) and a nominal reaction rate library (gray band) for the best-fit astrophysical conditions of Meisel (2018).

to impact the X-ray burst light curve, shown in Figure 1, and resultant ash abundances. Listed in order of multi-zone light curve impact according to Cyburt et al. (2016):

1. $^{15}\text{O}(\alpha, \gamma)^{19}\text{Ne}$ was decreased by a factor of 10 based on the lower-bound from the most recent evaluation (Davids et al. 2011). This reaction is the location of breakout from the hot CNO cycle, which is β -limited and thereby concentrates abundances at ^{14}O and ^{15}O , into the rp -process.
2. $^{59}\text{Cu}(p, \alpha)^{56}\text{Ni}^1$ was increased by a factor of 100. This reaction competes with $^{59}\text{Cu}(p, \gamma)$ in the NiCu cycle, working to keep material within the cycle and prolonging the effective waiting-point at this location.
3. $^{59}\text{Cu}(p, \gamma)^{60}\text{Zn}$ was decreased by a factor of 100. This reaction is the avenue for breakout from the aforementioned NiCu cycle.
4. $^{61}\text{Ga}(p, \gamma)^{62}\text{Ge}$ was decreased by a factor of 100. This reaction connects the NiCu and ZnGa cycles by proton-capture onto the ^{61}Ga abundance maintained by the $(p, \gamma) - (\gamma, p)$ equilibrium between ^{60}Zn and ^{61}Ga . This provides a bypass for the relatively long ^{60}Zn half-life.
5. $^{22}\text{Mg}(\alpha, p)^{25}\text{Al}$ was decreased by a factor of 10. This reaction occurs at a branch-point, competing with the rather slow ^{22}Mg β^+ -decay and, at low temperatures, the $^{22}\text{Mg}(p, \gamma)$ reaction.
6. $^{14}\text{O}(\alpha, p)^{17}\text{F}$ was decreased by a factor of 10 based roughly on the systematic change in the reaction rate caused by assuming constructive or destructive interference between resonances (Hu et al. 2014) and on the fact that some disagreement exists as to relevant resonance properties (Fortune 2012). This reaction connects hot CNO cycles, speeding up the breakout process marking burst ignition.
7. $^{23}\text{Al}(p, \gamma)^{24}\text{Si}$ was decreased by a factor of 30² based on the uncertainty evaluation of Cyburt et al. (2016) using the ^{24}Si structure information from Schatz et al. (1997). This reaction enables the (p, γ) path from the ^{22}Mg branch-point at high temperatures by proton-capture on the ^{23}Al present due to $(p, \gamma) - (\gamma, p)$ equilibrium.
8. $^{18}\text{Ne}(\alpha, p)^{21}\text{Na}$ was increased by a factor of 30 based on the uncertainty evaluation of Cyburt et al. (2016) using the experimental results of Matic et al. (2009). A smaller uncertainty has been determined by a more recent reaction rate evaluation (Mohr et al. 2014); however, a subsequent evaluation of the ^{22}Mg structure (Shamsuzzoha Basunia 2015) includes an additional 1^- resonance in the Gamow window that would likely increase the reaction rate if present. This reaction rate is a breakout reaction from the hot CNO cycle due to the high ^{18}Ne concentration that results from its β -limiting role.
9. $^{63}\text{Ga}(p, \gamma)^{64}\text{Ge}$ was decreased by a factor of 10. This reaction is the avenue for breakout from the aforementioned ZnGa cycle.
10. $^{19}\text{F}(p, \alpha)^{16}\text{O}$ was increased by a factor of 10. This reaction competes with the cold CNO cycle breakout reaction $^{19}\text{F}(p, \gamma)$ and the reverse rate is an influential helium-burning reaction in burning regions lacking hydrogen.
11. $^{12}\text{C}(\alpha, \gamma)^{16}\text{O}$ was increased by a factor of 1.25 to approximate the uncertainty band found by a recent analysis of this reaction rate (deBoer et al. 2017). This reaction is a major source of energy generation where hydrogen is absent, such as the reheated burst ashes below the region of burst ignition.
12. $^{26}\text{Si}(\alpha, p)^{29}\text{P}$ was increased by a factor of 10 based on the systematic uncertainty of Almaraz-Calderon et al. (2012). This reaction occurs at a branch-point, competing with the $^{26}\text{Si}(p, \gamma)$ reaction.
13. $^{17}\text{F}(\alpha, p)^{20}\text{Ne}$ was increased by a factor of 10. This reaction competes with $^{17}\text{F}(p, \gamma)$, which bridges the CNO cycle into the hot CNO cycle.
14. $^{24}\text{Mg}(\alpha, \gamma)^{28}\text{Si}$ was increased by a factor of 10. Like $^{12}\text{C}(\alpha, \gamma)$, this reaction generates energy in hydrogen-depleted zones during the burst.
15. $^{57}\text{Cu}(p, \gamma)^{58}\text{Ni}$ was decreased by a factor of 10³. This reaction occurs on the equilibrium abundance of ^{57}Cu , which is in $(p, \gamma) - (\gamma, p)$ equilibrium with ^{56}Ni during most of the burst, expediting the flow out of this strong waiting-point nucleus (Langer et al. 2014).
16. $^{63}\text{Ga}(p, \alpha)^{60}\text{Zn}$ was decreased by a factor of 100. This reaction keeps material within the aforementioned ZnGa cycle.
17. $^{17}\text{F}(p, \gamma)^{18}\text{Ne}$ was increased by a factor of 6.33 based on the uncertainty estimate of Cyburt et al. (2016), which was updated from the evaluation of Iliadis et al. (2010). This reaction connects the CNO and hot CNO cycles.
18. $^{40}\text{Sc}(p, \gamma)^{41}\text{Ti}$ was decreased by a factor of 100. This reaction allows material to flow beyond the ^{39}Ca waiting-point, which is due to $Z = 20$ magicity, by proton-capture on the equilibrium abundance of ^{40}Sc .
19. $^{48}\text{Cr}(p, \gamma)^{49}\text{Mn}$ was decreased by a factor of 100. This reaction pushes material beyond the ^{48}Cr bottleneck that occurs due to prior reaction pathways leading to this relatively long-lived nucleus.

¹ Note: Cyburt et al. (2016) chose to write all positive Q -value (p, α) reactions as (α, p) reactions in their Table 2.

² While this work was in writing, we became aware of an updated reaction rate uncertainty from C. Langer et al. which has been submitted for publication. The one standard deviation uncertainty band for the new rate does not include the factor of 30 reduction from the nominal reaction rate used here.

³ A rate reduction factor of 100 was used by Cyburt et al. (2016) because their calculations were performed prior to Langer et al. (2014) reducing this rate uncertainty.

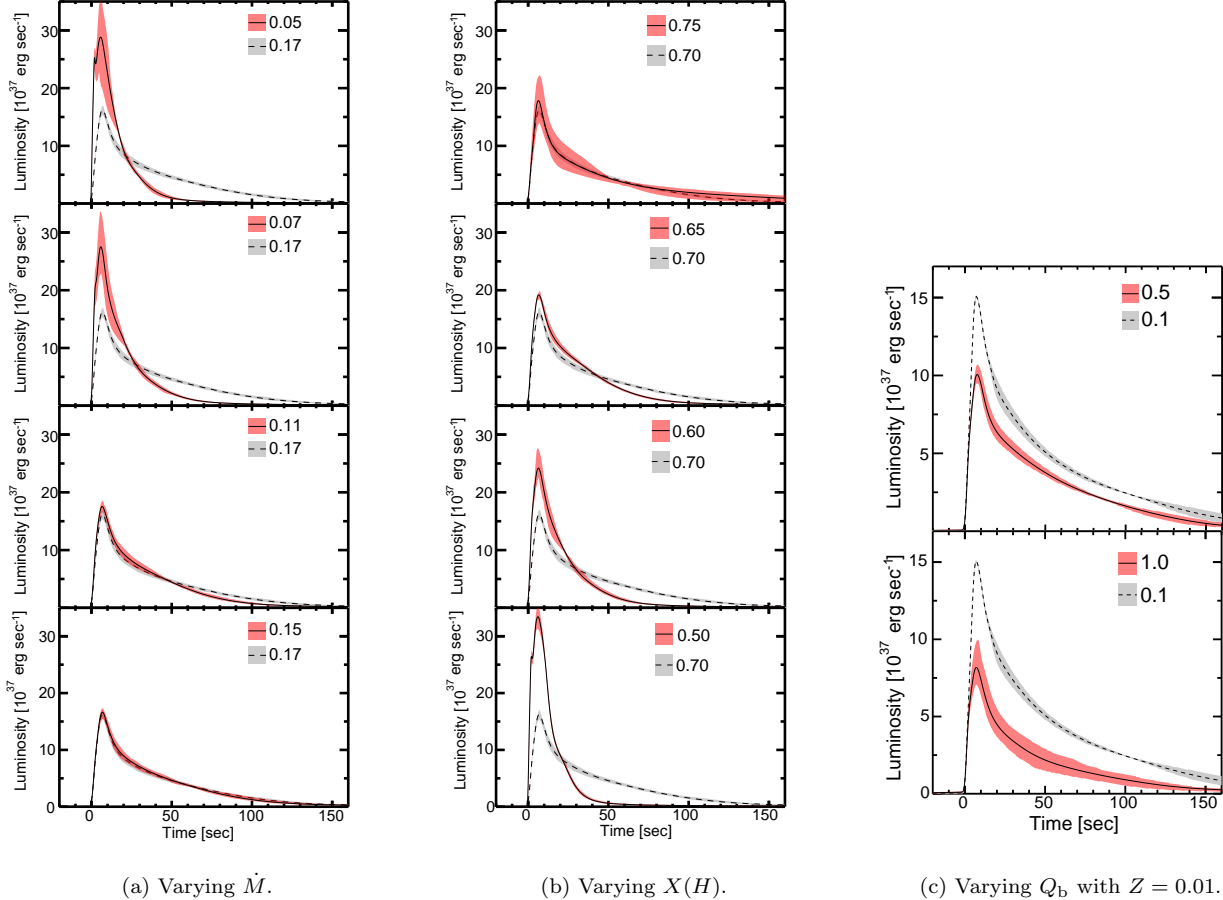


FIG. 2.— Calculated light curves for, unless otherwise stated, the conditions $\dot{M} = 0.17 \dot{M}_E$, $X(H) = 0.7$, $Z = 0.02$, and $Q_b = 0.1$ MeV/u. The legends indicate the value of the quantity being varied in that figure panel.

4. INFLUENCE ON LIGHT CURVE PROPERTIES

4.1. Quantitative Light Curve Features

The impact of astrophysical conditions and nuclear reaction rates on the X-ray burst light curve was quantified by assessing their influence on various light curve features. This approach provides a more nuanced view than only quantifying the overall deviation from one light curve to another using a sensitivity factor, as done in Cyburt et al. (2016). This also enables a closer comparison to the X-ray burst calculations of Lampe et al. (2016), who explored a large range of astrophysical conditions. The light curve features of interest here are the recurrence time Δt_{rec} , rise time t_{rise} , “10-to-10” time t_{10-10} , convexity \mathcal{C} , non-exponentiality \mathcal{E} , and the Gaussian fluence fraction f , each of which are described below.

Δt_{rec} is the average time between X-ray bursts, where the burst start is defined as the time when the luminosity passes over a defined threshold.

t_{10-10} is the time between the points in the X-ray burst light curve rise and decay when the luminosity has risen above and declined below 10% of the peak luminosity for the averaged light curve. This is a metric for the overall duration of the burst, adopting the definition used in Cyburt et al. (2016).

\mathcal{C} was defined by Maurer & Watts (2008) to quantify

the shape of the rise of the X-ray burst light curve. It is calculated by the following procedure. First, the burst light curve rise is rescaled so that the luminosity at 10% of the peak luminosity is at a rescaled (time,luminosity) of (0,0) and the luminosity at 90% of the peak luminosity is at (10,10). \mathcal{C} captures the deviation from linearity of the rise by integrating the difference between the rescaled luminosity L' and a straight line: $\mathcal{C} = \int_0^{10} (L' - x) dx$.

We introduce \mathcal{E} in analogy to \mathcal{C} , but for the X-ray burst tail. To calculate this parameter, the burst light curve is rescaled so that the peak luminosity has a rescaled (time,luminosity) of (0,10) and the point in the X-ray burst tail that the luminosity is $1/e$ of the peak luminosity is defined as a (time,luminosity) of (10, $1/e$). As the goal of \mathcal{E} is to quantify the morphology of the tail in order to capture the deviation from exponential behavior, which has often been assumed for fitting purposes (in’t Zand et al. 2017), the integrated difference is mirrored at the $1/e$ point: $\mathcal{E} = \int_0^{10} (L' - 10e^{-x/10}) dx + \int_{10}^{50} (10e^{-x/10} - L') dx$.

An alternative prescription for the light curve tail comes from in’t Zand et al. (2017). These authors fit an observed light curve flux using a power-law to describe the cooling of the envelope and a Gaussian to describe the extra flux due to rp -process burning: $F(t) =$

$F(t_0) (t/t_0)^{-a} + (G/\sqrt{2\pi s}) e^{-t^2/2s^2}$, where $F(t_0)$, a , G , and s are fit to the data and t_0 is the time in the X-ray burst tail that the flux first drops below 55% of the peak flux. The rp -process contribution is quantified by the fraction f of the Gaussian fluence to the total fluence. In order to stay within the same order of magnitude for G as observed bursts, to calculate f we apply a redshift $1+z = 1.44$ and distance $d\xi_b^{1/2} = 6$ kpc to transform the simulated averaged light curves into an “observed” flux via $F = L/(4\pi\xi_b(1+z)d^2)$ and dilate time by a factor of $1+z$.

Other than f , each of the above quantities was calculated for individual bursts in a burst sequence and this information was used to determine an average and 68% confidence interval.

4.2. Impact of Astrophysical Conditions

The consequences for varying the accretion properties \dot{M} , $X(H)$, and Q_b are shown in Figures 2 and 3. These effects can mostly be understood by considering the way in which modifying an astrophysical condition alters the H/He fraction and the envelope temperature in between bursts, as these are the main two quantities impacting burst ignition (Galloway et al. 2004).

Qualitatively, it is apparent that lower \dot{M} , lower $X(H)$, and higher Q_b , relative to the best-fit calculations of Meisel (2018), all shorten the duration of the light curve. The former two modifications also increase the peak luminosity of the burst, while the latter decreases the peak luminosity. These changes can be understood by considering the stable burning occurring between bursts.

Decreasing \dot{M} results in a cooler envelope since Q_b scales with accretion rate. To compensate, a more He-rich environment is required to achieve burst ignition conditions. Δt_{rec} lengthens for lower \dot{M} since more hydrogen must be burned into helium to achieve the required He abundance. The more He-rich fuel will burn brighter and faster, since helium burning reactions are generally more temperature sensitive than hydrogen burning reactions. The faster burning is manifested by reduced t_{rise} and t_{10-10} , where the latter reduction is compounded by an absence of late time hydrogen burning. Increased \mathcal{C} for more He-rich burst conditions are likely due to an emphasis of the (α, p) -process in the reaction flow (Weinberg et al. 2006) and the flow favoring the slower (α, p) reactions over (p, γ) reactions at branch points due to the lower hydrogen abundance at burst ignition. \mathcal{E} is positive for lower $X(H)$, meaning the burst tail falls off faster than exponential, indicating a lack of late-time hydrogen burning. The decrease in f contains the same signature.

Directly reducing $X(H)$ makes for a more helium rich envelope, leading to most of the same consequences as just discussed. However, longer burning time between bursts is not required to build up the helium density required for burst ignition, so Δt_{rec} is far less sensitive to changes in $X(H)$. Interestingly, for the highest $X(H)$, f begins to turn-over although there is more hydrogen burning ongoing at late times, i.e. a more extensive rp -process.

Increasing Q_b has the effect of increasing the envelope temperature, which reduces the burning time required to achieve ignition, shortening Δt_{rec} . Since less

fuel is built-up between bursts, the bursts will be less energetic, exhibiting a lower peak luminosity, and have a shorter t_{10-10} . We speculate that the higher temperatures modify the reaction flow and therefore nuclear energy generation during the burst rise. This would lead to increased \mathcal{C} for higher Q_b . We leave the investigation of this phenomenon for a future work, but note that it limits the ability for an increased Q_b to allow for a decreased \dot{M} while still explaining Δt_{rec} of an observed bursting source. We discuss this further, as well as the consequences, in Section 4.4.

The changes in the X-ray burst light curve properties with \dot{M} are in good agreement with the behavior Lampe et al. (2016) calculated using KEPLER models, with the exception of Δt_{rec} . While the same qualitative behavior is observed between the two models, the KEPLER models generally have a shorter Δt_{rec} at a given \dot{M} and a weaker dependence of Δt_{rec} on \dot{M} . Resolving this discrepancy will require a detailed comparison of model assumptions.

4.3. Impact of Nuclear Reaction Rates

Figures 1 and 3 show the impact varied reaction rates have on quantitative features of the X-ray burst light curve for the baseline astrophysical conditions adopted here. Note that the results of all 19 rate variations are not shown in Figure 3, rather only those that have a significant impact on the quantity under consideration.

Δt_{rec} is reduced by 15% for the rate variations $^{15}\text{O}(\alpha, \gamma)/10$ and $^{14}\text{O}(\alpha, p)/10$, which can be compared to the 11% and 7% respective reductions found by Cyburt et al. (2016) for similar (but not identical) astrophysical conditions.

t_{rise} is only significantly altered by $^{23}\text{Al}(p, \gamma)/30$, with an increase of 15%.

t_{10-10} is decreased by 20% for $^{15}\text{O}(\alpha, \gamma)/10$ and $^{59}\text{Cu}(p, \gamma)/100$ and increased by 10% for $^{61}\text{Ga}(p, \gamma)/100$ and $^{23}\text{Al}(p, \gamma)/30$.

\mathcal{C} is sensitive to several reaction rate variations, ranging from 225% of the baseline value for $^{15}\text{O}(\alpha, \gamma)/10$ to a 150% reduction for $^{23}\text{Al}(p, \gamma)/30$. Other notable sensitivities are an increase by 75% for $^{14}\text{O}(\alpha, p)/10$, a decrease by 25% for $^{18}\text{Ne}(\alpha, p) \times 30$, and an increase by 25% for $^{24}\text{Mg}(\alpha, \gamma) \times 10$.

\mathcal{E} also shows a marked sensitivity to several rate variations. The largest and second largest \mathcal{E} correspond to $^{59}\text{Cu}(p, \gamma)/100$ and $^{22}\text{Mg}(\alpha, p)/10$, respectively. The most negative \mathcal{E} corresponds to $^{23}\text{Al}(p, \gamma)/30$, while the second most negative \mathcal{E} is due to $^{61}\text{Ga}(p, \gamma)/100$.

f is also altered by $^{23}\text{Al}(p, \gamma)/30$, $^{59}\text{Cu}(p, \gamma)/100$, and $^{61}\text{Ga}(p, \gamma)/100$; however, it decreases for each rate variation. As such, though f and \mathcal{E} describe the evolution of the burst light curve tail, it appears they contain complementary information.

Overall, the reaction rate sensitivities are qualitatively similar to those seen for the multizone calculations of Cyburt et al. (2016). However, that work did not report most of the quantitative light curve features under study here and so a detailed comparison is generally not possible. Furthermore, some differences could be attributed to the somewhat lower accretion rate, $0.1 \dot{M}_E$, adopted in that work.

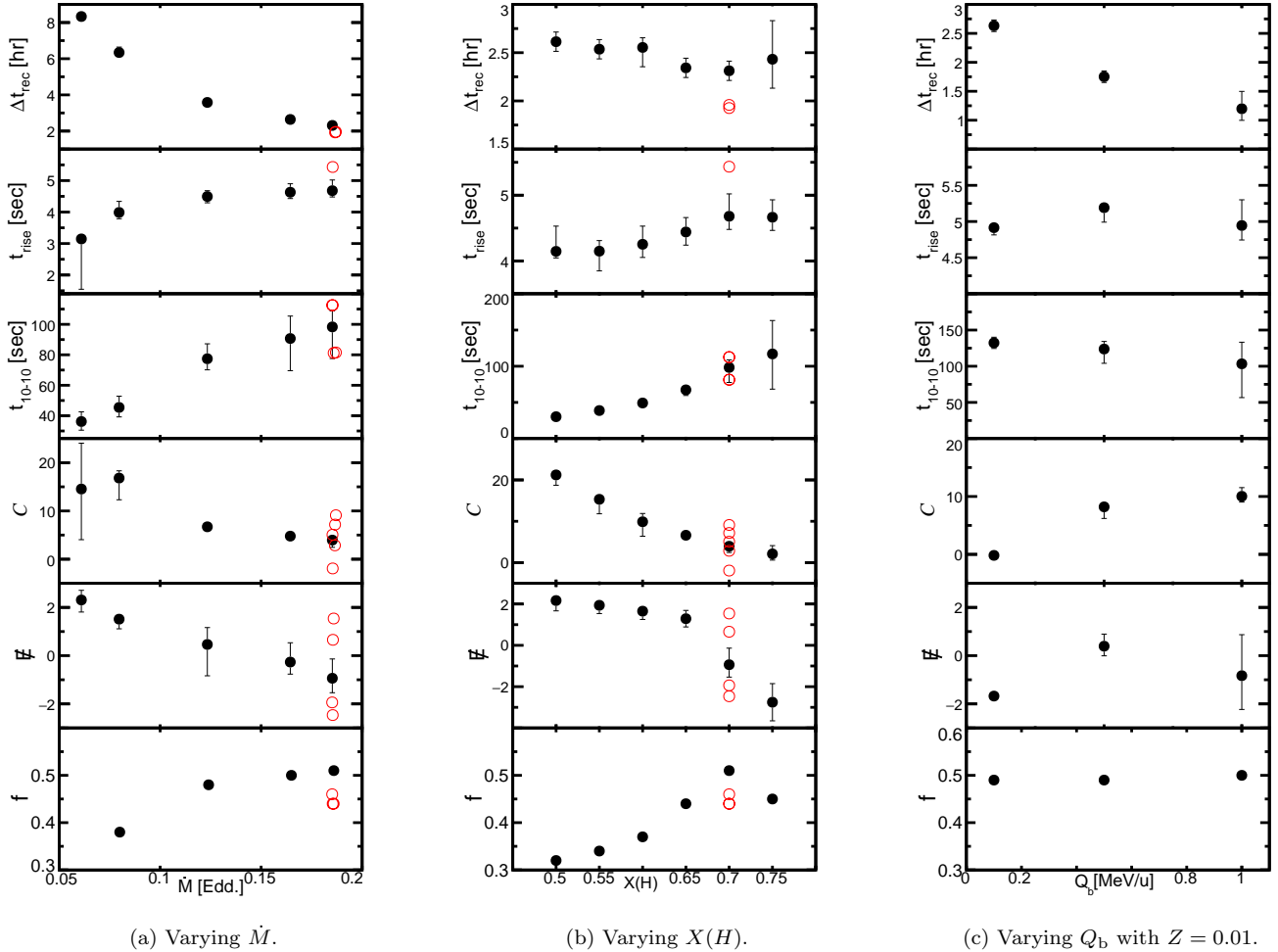


FIG. 3.— Quantitative features for the light curves shown in Figure 2 (solid black circles) and cases from Figure 1 that significantly deviated from the baseline result (open red circles), as discussed in Section 4.3.

4.4. Discussion of Relative Light Curve Impacts

Comparing the relative impacts of varied astrophysical conditions and nuclear reaction rates on the features of the X-ray burst light curve enables us to assess the robustness of constraints on astrophysical conditions derived from model-observation comparisons, e.g. from Heger et al. (2007); Galloway et al. (2017); Meisel (2018). It is important to note that both the shape and Δt_{rec} must be reproduced and, to limit the degeneracy of acceptable solutions, this should be done for bursting epochs at multiple accretion rates if possible (Meisel 2018).

From Figure 3 it is apparent that Δt_{rec} is most sensitive to changes in \dot{M} and Q_b . Considering only Δt_{rec} , one can see that the (\dot{M}, Q_b) combinations $(0.17 \dot{M}_E, 0.1 \text{ MeV/u})$ and $(0.11 \dot{M}_E, 1.0 \text{ MeV/u})$ would arrive at a similar result. However, when including the burst morphology, we see that this change in \dot{M} leaves C largely unchanged, but modifies \bar{E} substantially. In opposition, this change in Q_b significantly changes C and leaves \bar{E} more or less unaltered. One could imagine that the C increase from increasing Q_b could be mitigated by a modification of $X(H)$. However, it is apparent that an $X(H)$ increase

would only modestly reduce C while also substantially reducing \bar{E} . As such, to explain a source such as GS 1826-24, there appears to be a unique solution in terms of \dot{M} , $X(H)$, and Q_b , which Meisel (2018) used to demonstrate that shallow heating in neutron star outer layers can be constrained with X-ray burst light curve model-observation comparisons.

It is natural to ask whether reaction rate variations could modify these conclusions, resulting in a different set of best-fit astrophysical conditions. For this analysis we turn to the unfilled red circles of Figure 3. The first thing to notice is that no rate variation substantially changes Δt_{rec} , so the two (\dot{M}, Q_b) solutions explaining this observable are robust. Then, to modify the conclusion about which of these solutions is the best-fit, a reduction to C would be required, *while leaving other observables unchanged*. The only candidate for this is the rate variation $^{23}\text{Al}(p, \gamma)/30$. However, this rate variation also increases Δt_{rise} , increases t_{10-10} , and decreases \bar{E} . Therefore, it appears that the constraints on the astrophysical conditions involving accretion are robust.

It is unlikely this conclusion would be altered by incorporating the affects of flame spreading on the neutron

star surface, as this phenomenon will primarily impact only the light curve rise (Maurer & Watts 2008). Similarly, while a modification of the assumed surface gravitational redshift could change Δt_{rise} and t_{10-10} in the same direction (See Section 6), this light curve compression/stretching would rescale the decay but not alter \dot{E} . However, it is possible that different rate sensitivities for the higher Q_b conditions may open-up alternative solutions to matching the observed GS 1826-24 light curve, so a definite conclusion would require a nuclear reaction rate sensitivity study for those conditions. Furthermore, as this analysis is limited to explaining observed bursts for GS 1826-24, it cannot be certain that the accretion conditions for other sources would be able to be constrained in this way to the degree achieved here. Another caveat is that extra mixing processes in the neutron star outer layers may alter Δt_{rec} for a set of accretion conditions, though work considering this phenomenon is still in the exploratory phase (Cavecchi et al. 2017).

While we find nuclear reaction rate variations do not modify the conclusions about accretion properties for GS 1826-24 drawn from model-observation comparisons, this does not mean that reaction rate uncertainties are inconsequential for this source. In the following section we show that they are of consequence for neutron star crust properties. In Section 6, we demonstrate that nuclear reaction rate uncertainties have significant consequences for mass-radius constraints which can be extracted from X-ray burst model-observation comparisons.

5. INFLUENCE ON NUCLEOSYNTHESIS

Upon reproducing an observed burst light curve, it is natural to surmise that the nucleosynthesis for a particular source has also been reproduced. This could provide constraints on the composition and thermal structure of the outer layers of the neutron star, which would be of use when modeling other accreting neutron star observables (Deibel et al. 2016; Meisel & Deibel 2017). We therefore also investigate the impact of nuclear reaction rate uncertainties on the X-ray burst ash composition and compare this to the impact of modified astrophysical conditions.

5.1. Surface Abundances

Ash abundances were extracted after the last burst in the burst sequence, i.e. after $\sim 10 - 20$ bursts, for a consistent connection to the averaged light curve. However, we note that we observe the burst abundances converge after ~ 4 bursts. Mass fractions $X(A)$ for species of nuclear mass A were calculated by averaging over envelope layers that no longer experienced hydrogen or helium burning, following the approach of Cyburt et al. (2016); Meisel & Deibel (2017).

Figure 4 and Table 1 show the ash abundance distributions corresponding to the calculated light curves of Figure 2. Qualitatively, decreasing \dot{M} , decreasing $X(H)$, and increasing Q_b all reduce the extent of the ash distribution to lower- A material.

For the lowest \dot{M} modeled here, $X(A)$ rapidly falls off after $A = 60$, with steadily decreasing resurgences for the $A = 60 + 4n$ sequence, where n is an integer. The $X(A)$ distribution steadily fills in up to $A \sim 100$ for increasing \dot{M} , washing-out the $A = 4n$ signature for

$A > 60$. This increase comes at the expense of $X(A)$ for lower- A nuclides. It is notable that lower \dot{M} results in a larger $X(12)$, as current models have difficulty explaining the amount of ^{12}C required to ignite X-ray superbursts. Though all models fall far short of the $X(^{12}\text{C}) \gtrsim 20\%$ required to reconcile superburst models with observations (Cumming et al. 2006). These findings are consistent with lower \dot{M} resulting in more helium-rich bursts, therefore favoring α -capture reactions and as a result nuclei with $A = 4n$.

Unsurprisingly, directly lowering $X(H)$ of the accreted material leads to similar behavior in the ash composition. For $X(H) = 0.75$, which is just above the solar surface value, a significant enhancement for $A \gtrsim 80$ occurs, including a three orders of magnitude increase for $X(100)$.

Increasing Q_b over the range explored here has a more modest impact than the changes we observe for our \dot{M} and $X(H)$ variations. The reduction in high- A abundances is likely due to the absence of fuel left to burn late in the burst evolution because of the reduced fuel build-up time between bursts. We note that increased Q_b leads to increased $X(12)$, in qualitative agreement with Reichert et al. (2017), though calculation details are too different for a more direct comparison.

The different extent of the ash distributions in A can be seen when examining the flow of nucleosynthesis in the rp -process. The integrated flow for converting isotope i to isotope j is $\mathcal{F}_{ij} = \int (\dot{Y}_{i \rightarrow j} - \dot{Y}_{j \rightarrow i}) dt$ where the integral runs over the full burst time and $\dot{Y}_{i \rightarrow j}$ is the rate that the abundance of isotope i is depleted by reactions converting i to j . \mathcal{F}_{ij} for the models best reproducing GS 1826-24, with $X(H)$ increased to 0.75, and \dot{M} lowered to $0.07 \dot{M}_E$ are shown in Figure 6 for demonstration purposes. The different flows highlight the fact that reaction rate sensitivities may be quite different for different astrophysical conditions.

Examples for the impact of nuclear reaction rate variations on the surface ash composition are shown in Figure 5, where the composition for all rate variations of Section 3 are given in Tables 2 and 3. Comparing to Figure 4, it is apparent that rate variations have a comparable impact to modest changes in the accretion conditions. Nonetheless, for some reactions orders of magnitude changes in $X(A)$ can be observed at the high and low- A edges of the composition distribution and, for several other reactions, local changes near A of the reactant isotope can be observed. These local changes can often far exceed the variation in $X(A)$ due to varied accretion conditions, e.g. $A = 59$ for $^{59}\text{Cu}(p, \gamma)/100$.

5.2. Crust Temperature and Composition

Ashes produced on the accreting neutron star surface are buried by subsequent accretion to higher densities. There they are steadily modified by nuclear reactions, resulting in some compositional structure and driving local heat sources and heat sinks (Lau et al. 2018). These modifications to the compositional and thermal structure ultimately influence the ignition of X-ray superbursts and the light curves of cooling transient neutron stars (Deibel et al. 2016; Meisel & Deibel 2017). Here we focus on heat sources and sinks which have previously been identified

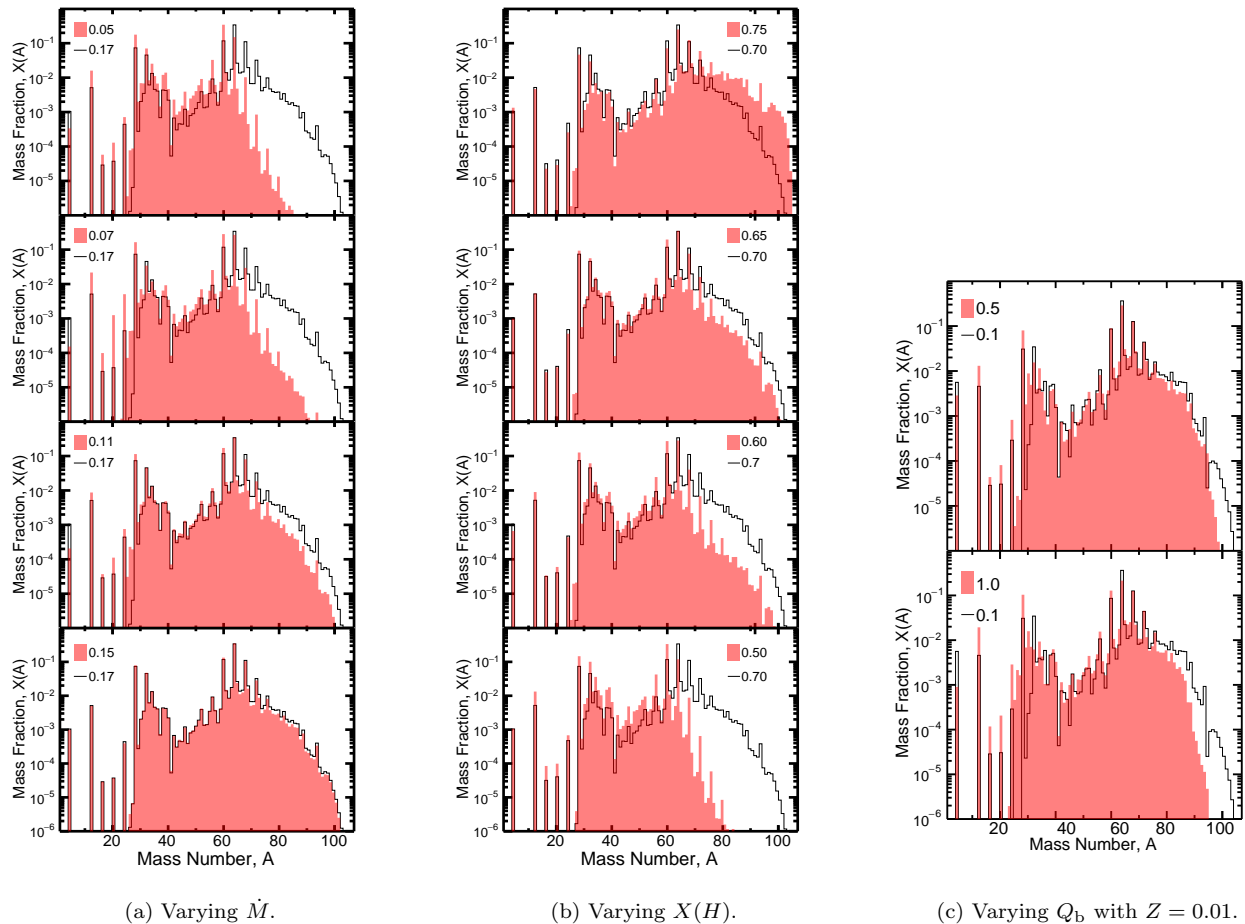


FIG. 4.— Ash compositions for model calculations corresponding to the light curves in Figure 2.

as significant and the composition of the neutron star inner crust, whose connection to the surface burning ashes has been recently calculated using detailed reaction network calculations.

Heating from electron-capture is strongest for even- A nuclides with a large odd-even mass staggering, since for these cases a significant fraction of the second electron-capture in a two electron-capture sequence can proceed through excited states that then deposit a large amount of energy through γ -deexcitation. Among these, $^{66}\text{Ni} \rightarrow ^{66}\text{Fe}$, $^{66}\text{Fe} \rightarrow ^{66}\text{Cr}$, and $^{64}\text{Cr} \rightarrow ^{64}\text{Ti}$ stand out (Gupta et al. 2007). We find nuclear reaction rate uncertainties could allow for at most a factor of ~ 2 change in $X(64)$ and $X(66)$. $X(64)$ shows a similar level of stability across the range of astrophysical conditions modeled here, though $X(66)$ can be substantially reduced from the possible percent level for particularly helium-rich bursts.

Local heat sinks can be formed in the neutron star outer layers by cycling between electron captures and β^- -decays, which predominantly occurs for odd- A nuclides in regions of deformation with particularly small odd-even mass staggering (Schatz et al. 2014; Meisel et al. 2015). The potential for this urca cooling process has been identified for $A = 29, 31, 33, 55, 57, 59, 63, 65, 103$, and 105 , where $X(A) \sim 5 \times 10^{-3}$ or greater are re-

quired for significant cooling (Meisel & Deibel 2017). We find that $^{15}\text{O}(\alpha, \gamma)/10$ enhances $X(29)$ and $X(31)$ to this level. $X(33)$, $X(55)$, and $X(57)$ are always at or near the threshold of significant cooling for all rate variations. $X(59)$ is generally below the threshold, though is boosted to $X(A) \sim 5 \times 10^{-2}$ by $^{59}\text{Cu}(p, \gamma)/100$. $X(63)$ and $X(65)$ are at the percent level for all rate variations, though it is notable that $X(63)$ is doubled from the nominal value by $^{61}\text{Ga}(p, \gamma)/100$, likely because this variation effectively stalls material within the ZnGa cycle. $X(103)$ and $X(105)$ are sensitive to a number of the nuclear reaction rate variations explored here, though they are orders of magnitude too small to result in significant urca cooling for each of these calculations.

In the neutron star inner crust the thermal conductivity is dominated by electron-ion impurity scattering. As such, the inner crust impurity is of particular interest. This is quantified using the variance of the charge distribution, which is known as the impurity parameter Q_{imp} . $Q_{\text{imp}} = \frac{1}{n_{\text{ion}}} \sum_j n_j (Z_j - \langle Z \rangle)^2$, where n_{ion} is the ion number density, n_j is the number density of species with atomic number Z_j , and $\langle Z \rangle$ is the average atomic number of the composition. We cannot directly infer Q_{imp} from the surface burning ashes, since crust reactions drastically modify the composition as it is buried

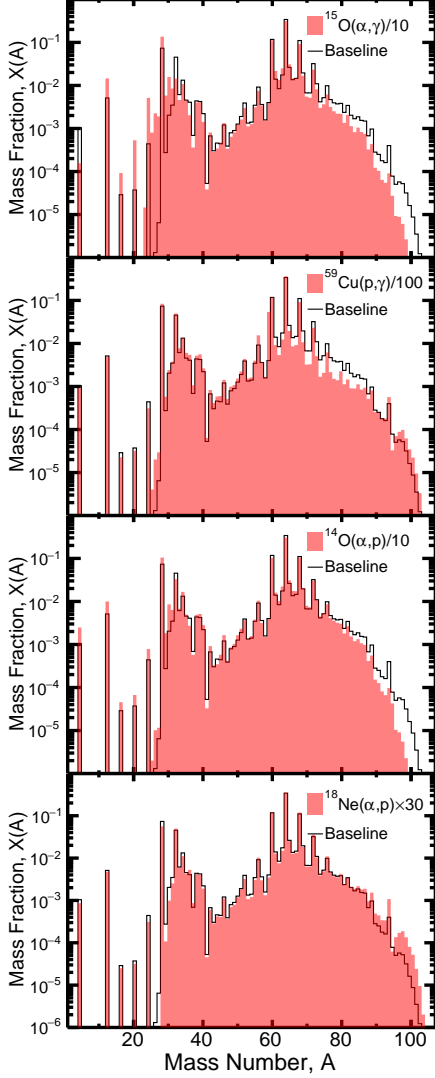
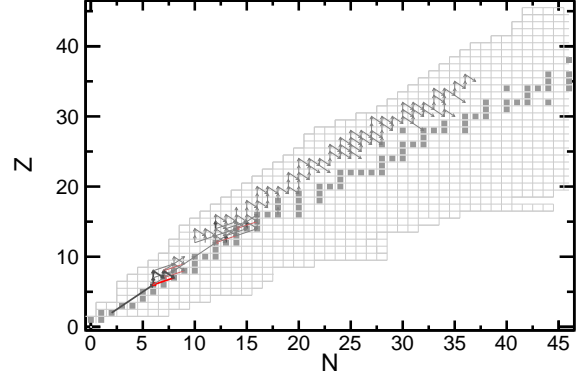


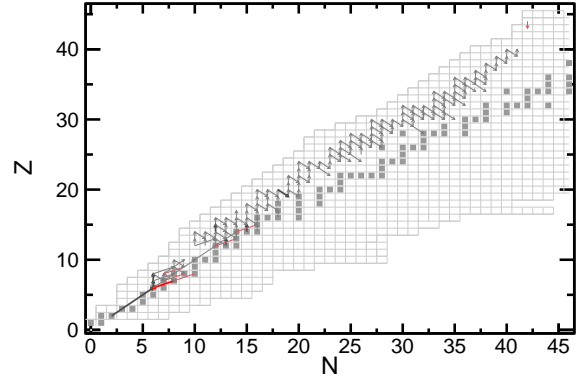
FIG. 5.— Ash compositions for example nuclear reaction rate variations.

to inner crust depths. However, Lau et al. (2018) found a correlation between the A of a nucleus at the surface and its corresponding equilibrium isotope in the crust. At the inner crust, material becomes concentrated into the $N = 28, 50,$ and 82 shell closures; for the finite range droplet mass model (FRDM) (Möller et al. 2018), these are ^{40}Mg , ^{70}Ca , and ^{116}Se . The surface to inner crust mapping they found was that $A < 28$ and $A = 29 - 55$ are funneled into $N = 28$, $A = 56 - 60$ are split between $N = 28$ and $N = 50$, $A = 61 - 101$ ultimately go to $N = 50$, and $A = 102 - 105$ are split between $N = 50$ and $N = 82$. For the cases where $X(A)$ are split between two magic numbers, Lau et al. (2018) note that the exact split depends on the neutron abundance and competing reaction rates.

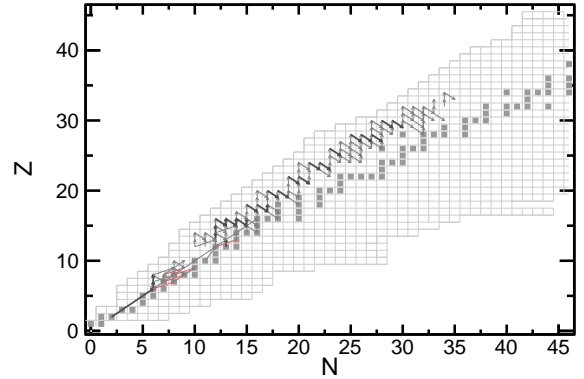
We calculate the inner crust impurity $Q_{\text{imp}}^{\text{inner}}$ resulting from our surface abundance distributions using the mapping just described, where we use the crude approximation that splitting between two magic numbers is half and half. These results are in the last row of Tables 1–3. To



(a) Baseline.



(b) $X(H) = 0.75$.



(c) $\dot{M} = 0.07 \dot{M}_E$.

FIG. 6.— \mathcal{F}_{ij} for example cases, where the arrow indicates the direction $i \rightarrow j$. Thick lines correspond to $\mathcal{F}_{ij} > 1$ mol/g, whereas thin lines correspond to $10^{-1.5} < \mathcal{F}_{ij} < 1$ mol/g. (p, α) , (γ, p) , and (γ, α) reactions are indicated with red lines for convenience.

TABLE 3
SAME AS TABLE 2, BUT FOR THE REMAINING RATE VARIATIONS.

A	15	16	17	18	19
4	9.97E-04	1.74E-03	9.99E-04	1.01E-03	1.13E-03
12	4.77E-03	4.13E-03	4.94E-03	5.04E-03	5.21E-03
13	7.15E-12	3.76E-12	1.60E-14	9.83E-14	5.40E-15
16	3.07E-05	2.35E-05	2.81E-05	2.99E-05	2.96E-05
19	5.13E-13	1.02E-13	1.55E-14	3.15E-17	3.18E-13
20	7.36E-05	6.32E-05	4.47E-05	3.88E-05	4.07E-05
21	1.09E-08	5.29E-09	6.16E-10	1.48E-10	2.85E-09
22	1.86E-08	5.94E-09	9.83E-10	9.24E-13	4.46E-10
23	3.20E-08	6.98E-08	1.73E-08	1.22E-09	2.28E-07
24	5.23E-04	3.61E-04	4.47E-04	4.09E-04	4.55E-04
25	2.83E-06	4.54E-06	1.77E-06	4.33E-07	1.31E-06
26	2.27E-05	5.72E-05	2.02E-05	6.94E-07	4.94E-06
27	3.60E-05	1.12E-04	4.13E-05	1.51E-06	6.88E-06
28	7.31E-02	6.31E-02	7.36E-02	7.42E-02	7.07E-02
29	3.22E-04	2.34E-04	3.94E-04	3.05E-04	2.71E-04
30	1.90E-03	1.20E-03	1.92E-03	1.80E-03	2.08E-03
31	3.35E-03	2.75E-03	3.38E-03	3.36E-03	3.58E-03
32	4.60E-02	5.25E-02	4.44E-02	4.44E-02	4.62E-02
33	6.17E-03	6.15E-03	6.14E-03	6.08E-03	6.62E-03
34	1.25E-02	1.14E-02	1.26E-02	1.25E-02	1.39E-02
35	4.48E-03	4.36E-03	4.54E-03	4.39E-03	4.88E-03
36	4.22E-03	5.25E-03	4.18E-03	3.99E-03	4.40E-03
37	7.12E-04	8.71E-04	7.02E-04	6.89E-04	7.54E-04
38	4.12E-03	4.21E-03	4.19E-03	4.04E-03	4.64E-03
39	3.99E-03	4.18E-03	3.99E-03	6.07E-03	4.38E-03
40	2.15E-03	2.03E-03	2.17E-03	2.63E-03	2.11E-03
41	5.28E-05	5.60E-05	5.46E-05	5.58E-05	4.91E-05
42	6.22E-04	6.32E-04	6.25E-04	6.81E-04	7.10E-04
43	3.09E-04	3.21E-04	2.95E-04	3.24E-04	3.26E-04
44	4.67E-04	4.58E-04	4.71E-04	4.93E-04	4.52E-04
45	4.16E-04	4.33E-04	4.24E-04	4.41E-04	4.33E-04
46	1.13E-03	1.14E-03	1.13E-03	1.07E-03	1.29E-03
47	4.12E-04	3.90E-04	3.91E-04	3.97E-04	4.07E-04
48	7.81E-04	7.63E-04	7.96E-04	7.95E-04	7.88E-03
49	8.89E-04	8.36E-04	8.92E-04	8.72E-04	9.38E-04
50	1.23E-03	1.23E-03	1.22E-03	1.16E-03	1.09E-03
51	1.86E-03	1.89E-03	1.84E-03	1.74E-03	1.48E-03
52	3.89E-03	3.80E-03	3.94E-03	4.00E-03	2.06E-03
53	1.32E-03	1.28E-03	1.33E-03	1.34E-03	8.05E-04
54	1.39E-03	1.34E-03	1.38E-03	1.32E-03	1.09E-03
55	3.43E-03	3.36E-03	3.43E-03	3.27E-03	2.81E-03
56	1.36E-02	1.10E-02	8.81E-03	8.15E-03	8.79E-03
57	4.15E-03	3.26E-03	3.63E-03	3.63E-03	2.69E-03
58	1.62E-03	1.38E-03	1.57E-03	1.58E-03	1.25E-03
59	3.82E-03	3.87E-03	4.02E-03	3.95E-03	3.44E-03
60	1.14E-01	1.48E-01	1.17E-01	1.16E-01	1.13E-01
61	1.42E-02	1.30E-02	1.41E-02	1.42E-02	1.37E-02
62	8.49E-03	7.34E-03	8.36E-03	8.47E-03	8.18E-03
63	1.73E-02	1.53E-02	1.71E-02	1.71E-02	1.68E-02
64	3.43E-01	3.62E-01	3.46E-01	3.44E-01	3.36E-01
65	2.58E-02	2.21E-02	2.58E-02	2.59E-02	2.66E-02
66	1.33E-02	1.09E-02	1.33E-02	1.33E-02	1.38E-02
67	1.43E-02	1.18E-02	1.44E-02	1.47E-02	1.50E-02
68	1.11E-01	1.04E-01	1.12E-01	1.11E-01	1.14E-01
69	1.93E-02	1.46E-02	1.93E-02	1.93E-02	2.03E-02
70	6.56E-03	4.70E-03	6.44E-03	6.51E-03	7.06E-03
71	6.62E-03	4.81E-03	6.53E-03	6.64E-03	7.15E-03
72	3.19E-02	2.83E-02	3.20E-02	3.19E-02	3.32E-02
73	1.09E-02	7.75E-03	1.08E-02	1.08E-02	1.14E-02
74	4.08E-03	2.73E-03	3.99E-03	4.05E-03	4.43E-03
75	5.13E-03	3.40E-03	5.03E-03	5.08E-03	5.54E-03
76	9.69E-03	8.23E-03	9.58E-03	9.67E-03	9.98E-03
77	4.69E-03	3.43E-03	4.67E-03	4.72E-03	4.80E-03
78	3.93E-03	2.64E-03	3.86E-03	3.92E-03	4.11E-03
79	3.71E-03	2.50E-03	3.64E-03	3.71E-03	3.82E-03
80	3.74E-03	3.19E-03	3.65E-03	3.75E-03	3.76E-03
81	2.38E-03	1.86E-03	2.35E-03	2.42E-03	2.35E-03
82	3.48E-03	2.56E-03	3.42E-03	3.56E-03	3.43E-03
83	2.06E-03	1.58E-03	2.01E-03	2.12E-03	2.02E-03
84	1.68E-03	1.43E-03	1.62E-03	1.72E-03	1.65E-03
85	1.90E-03	1.75E-03	1.84E-03	1.97E-03	1.83E-03
86	1.60E-03	1.44E-03	1.56E-03	1.68E-03	1.53E-03
87	1.54E-03	1.51E-03	1.49E-03	1.61E-03	1.46E-03
88	6.95E-04	7.59E-04	6.59E-04	7.01E-04	6.51E-04
89	1.05E-03	1.22E-03	1.00E-03	1.03E-03	9.53E-04
90	3.17E-04	3.74E-04	2.97E-04	2.98E-04	2.77E-04
91	2.76E-04	3.60E-04	2.64E-04	2.58E-04	2.46E-04
92	2.03E-04	2.62E-04	1.91E-04	1.84E-04	1.76E-04
93	1.85E-04	2.57E-04	1.71E-04	1.62E-04	1.60E-04
94	4.91E-04	7.85E-04	4.53E-04	4.02E-04	4.28E-04
95	7.35E-05	8.49E-05	7.69E-05	7.04E-05	6.35E-05
96	6.17E-05	1.02E-04	5.74E-05	4.88E-05	5.39E-05
97	7.32E-05	1.30E-04	6.83E-05	5.53E-05	6.41E-05
98	7.09E-05	1.46E-04	6.75E-05	4.97E-05	6.33E-05
99	4.51E-05	9.77E-05	4.58E-05	3.13E-05	4.23E-05
100	2.32E-05	5.53E-05	2.49E-05	1.53E-05	2.29E-05
101	1.21E-05	3.56E-05	1.36E-05	7.14E-06	1.30E-05
102	4.53E-06	1.59E-05	5.49E-06	2.43E-06	5.32E-06
103	1.44E-06	5.95E-06	1.91E-06	6.94E-07	1.82E-06
104	2.58E-07	1.24E-06	3.67E-07	1.18E-07	3.33E-07
105	1.14E-08	5.91E-08	1.72E-08	4.58E-09	1.38E-08
$Q_{\text{imp}}^{\text{inner}}$	13.0	13.7	12.9	12.9	13.1

be clear, a precise calculation would require use of a crust reaction network for varied astrophysical conditions and nuclear mass models. Nonetheless, these calculations are informative as a first approximation to the impact of nuclear reaction rate uncertainties and accretion conditions

on the inner crust impurity. We find $10 \lesssim Q_{\text{imp}}^{\text{inner}} \lesssim 16$ for all modeled conditions. The impurity is smallest for the most helium-rich conditions, increasing for moderately helium-rich bursts, and decreasing again for the most hydrogen-rich bursts. This is because the ashes from helium-rich bursts have a large fraction of nuclides that become $N = 28$ in the inner crust, whereas more hydrogen-rich bursts result in a larger fraction of $N = 50$. $Q_{\text{imp}}^{\text{inner}}$ is largest in the intermediate region. The nuclear reaction rate variations explored here can have a comparable impact on $Q_{\text{imp}}^{\text{inner}}$. Specifically, $\gtrsim 10\%$ enhancements are observed for $^{59}\text{Cu}(p, \alpha) \times 100$, $^{59}\text{Cu}(p, \gamma)/100$, and $^{61}\text{Ga}(p, \gamma)/100$. Each of these reaction rate variations boost $X(A)$ in the split region $A = 56 - 60$ and so the impact noted here may be an artifact of the adopted splitting ratio.

6. INFLUENCE ON THE NEUTRON STAR MASS-RADIUS RATIO DERIVED FROM MODEL-OBSERVATION COMPARISONS

In Section 4.4, it was shown that relatively tight constraints can be placed on the accretion conditions for GS 1826-24 based on reproducing the observed light curve shape and recurrence time over a range of accretion rates. This restricts the number of free parameters used to reproduce the observed light curve, which therefore reduces the phase space for remaining free parameters. Namely, we can now extract constraints for $d\xi_b^{1/2}$ and $1+z$. This procedure was described by Meisel (2018), but is briefly repeated here for completeness. We then demonstrate how these constraints are sensitive to uncertainties in nuclear reaction rates and how this sensitivity translates into an uncertainty on the extracted neutron star mass-radius ratio. Note, the $1+z$ determination may be systematically altered by astrophysical effects, such as the flame spreading on the neutron star surface, as pointed out by Zamfir et al. (2012). As such *one should focus on the relative change of $1+z$ with modified nuclear reaction rates, rather than on the absolute determination of $1+z$.*

6.1. Model-Observation Comparison of the Light Curve Shape

Observed light curve data for GS 1826-24 come from the analysis of the data in the Multi-Instrument Burst Archive (MINBAR)⁴ described in Galloway et al. (2017). They took individual burst light curves observed over a bursting epoch with the Rossi X-ray Timing Explorer (Galloway et al. 2004, 2008), aligned them in time, and obtained an average flux at each time, which is adopted as the observed light curve.

The simulated light curve is altered for an assumed $d\xi_b^{1/2}$ and $1+z$ to create $F(\tilde{t}) = L(\tilde{t})/(4\pi\xi_b(1+z)d^2)$, where F is the flux, L is the simulated luminosity, and $\tilde{t} = (1+z)t$ is the redshifted time (Galloway et al. 2017). The neutron star mass and radius adopted for the simulations correspond to $(1+z) = 1.26$, so in this sense choosing other redshifts is inconsistent. However, in practice burst ignition properties are insensitive to modest changes in the neutron star mass M_{NS} and radius R_{NS} , and therefore $(1+z)$ (Ayasli & Joss 1982; Zamfir et al.

⁴ <https://burst.sci.monash.edu/minbar/>

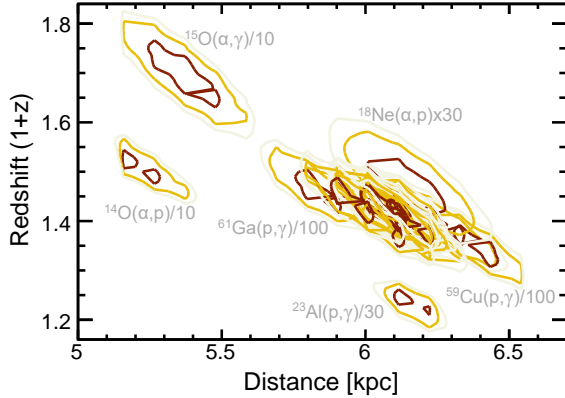


FIG. 7.— 68% (red lines), 95% (yellow lines), and 99% (gray lines) confidence intervals for the distance-redshift determination performed comparing light curves shown in Figure 1 to the GS 1826-24 2007 bursting epoch. Cases significantly deviating from the result for the baseline calculation are labeled.

2012). Finally, to compare to the observed light curve, a time shift δt is applied to the simulated light curve to obtain the minimum χ^2_{red} for a given combination of $d\xi_b^{1/2}$ and $1+z$.

We calculate χ^2_{red} using the 50 s of the light curve following thermonuclear runaway⁵ over the phase space $4.0 \leq d\xi_b^{1/2} \leq 8.1$ kpc in steps of 0.1 kpc, $1.16 \leq (1+z) \leq 1.84$ in steps of 0.01, and $0.2 \leq \delta t \leq 0.8$ s in steps of 0.1 s. See Figure 3 of Meisel (2018) for an example of the χ^2_{red} surface for the baseline reaction rate library. We assume our uncertainties for the parameters $d\xi_b^{1/2}$ and $1+z$ are Gaussian in order to convert between $\Delta\chi^2$ from the minimum χ^2 and a confidence interval so that we can more easily compare χ^2_{red} surfaces obtained for different model calculations (Press et al. 1992).

6.2. Impact of Nuclear Reaction Rates on the Extracted Distance and Redshift

The technique of the previous subsection was applied using each of the model calculations shown in Figure 1. The resulting confidence intervals for $d\xi_b^{1/2}$ and $1+z$ are shown in Figure 7. We identify six reaction rate variations which result in significantly different $d\xi_b^{1/2}$ and/or $1+z$ compared to the baseline calculation: $^{15}\text{O}(\alpha, \gamma)/10$, $^{14}\text{O}(\alpha, p)/10$, $^{18}\text{Ne}(\alpha, p) \times 30$, $^{23}\text{Al}(p, \gamma)/30$, $^{59}\text{Cu}(p, \gamma)/100$, and $^{61}\text{Ga}(p, \gamma)/100$. That these are the influential rates is unsurprising, due to their impact on t_{rise} , \mathcal{C} , \mathcal{E} , and the peak flux.

Only $^{15}\text{O}(\alpha, \gamma)/10$ results in a significantly increased $1+z$. We can therefore determine that an increase of \mathcal{C} of $\sim 75\%$ or larger is consequential for the redshift determination. $^{23}\text{Al}(p, \gamma)/30$ results in a significant reduction in $1+z$ from the baseline result, which may be a combination of the increase in t_{rise} and decrease in \mathcal{C} . Nonetheless, the absence of a significantly reduced $1+z$

⁵ The absolute $1+z$ is sensitive to this range, for instance shifting downward by ~ 0.05 when the fit-range is extended to cover the 150 s following thermonuclear runaway. However, the relative effect of the reaction rate variations is not significantly changed.

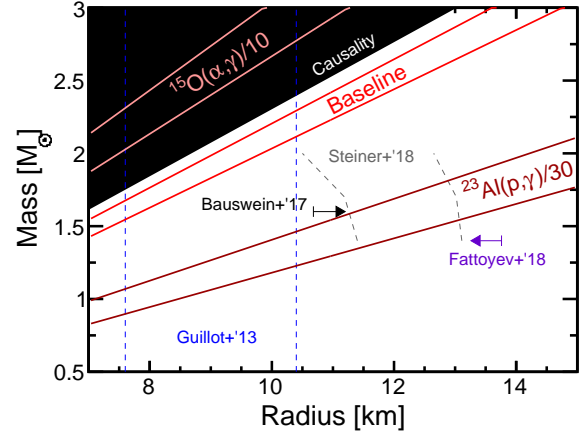


FIG. 8.— $M_{\text{NS}}/R_{\text{NS}}$ bands calculated from the $1+z$ 68% confidence intervals shown in Figure 7 for the baseline calculation and the two reaction rate variations resulting in the extremes for $1+z$. Constraints from other astrophysical observables (Guillot et al. 2013; Bauswein et al. 2017; Fattoyev et al. 2018; Steiner et al. 2018) are also shown and the unphysical region excluded by causality (Koranda et al. 1997) is shown in black.

for $^{18}\text{Ne}(\alpha, p) \times 30$ indicates that \mathcal{C} reductions of 25% or less are not consequential for the redshift determination. The influence of \mathcal{E} on the best-fit $1+z$ is apparent from $^{59}\text{Cu}(p, \gamma)/100$, for which an \mathcal{E} increase results in a reduced $1+z$, and $^{61}\text{Ga}(p, \gamma)$, for which a \mathcal{E} decrease results in an increased $1+z$. Since $^{22}\text{Mg}(\alpha, p)/10$ does not stand-out in this phase space, this sets a rough limit for an increase of \mathcal{E} that is consequential.

The deviations of $d\xi_b^{1/2}$ from the baseline result stem from the altered peak luminosity, with the exception of $^{15}\text{O}(\alpha, \gamma)/10$ for which the large increase in \mathcal{C} also plays a role. From Figure 1, it is clear that relatively modest alterations of the peak luminosity lead to quite different distance determinations. For instance, the $\sim 15\%$ decrease in peak luminosity for the calculation with $^{14}\text{O}(\alpha, p)/10$ reduces the best-fit distance by roughly the same amount.

6.3. Implications for Neutron Star Mass-Radius Ratio Constraints

The constraint for $1+z$ can directly be translated into a constraint on the neutron star mass and radius using the relationships described in the appendix of Lampe et al. (2016). The general relativistic neutron star mass and radius are related to the surface gravitational redshift by $1+z = 1/\sqrt{1 - 2GM_{\text{GR}}/(R_{\text{GR}}c^2)}$, where c is the speed of light and G is the gravitational constant. For the choice that the Newtonian mass is equal to the general relativistic mass $M_{\text{NS}} = M_{\text{GR}}$, then $R_{\text{GR}} = \sqrt{(1+z)}R_{\text{NS}}$. Therefore an uncertainty in $1+z$ can be converted into a band on the neutron star mass-radius diagram. This is shown for three calculations in Figure 8. It is clear the uncertainties in nuclear reaction rates prevent the use of model-observation comparisons to constrain $M_{\text{NS}}/R_{\text{NS}}$ to a useful degree. In particular, for the astrophysical conditions adopted here to reproduce the observed characteristics of GS 1826-24, improved uncertainties for $^{15}\text{O}(\alpha, \gamma)$ and $^{23}\text{Al}(p, \gamma)$ are es-

sential.

Eliminating the nuclear physics uncertainties that alter the determination of $1+z$ will open up the possibility to employ this light curve matching for a new constraint on $M_{\text{NS}}/R_{\text{NS}}$. Of course, the uncertainty contributions from astrophysical phenomena like flame spreading, e.g. the impact on \mathcal{C} from polar versus equatorial ignition (Maurer & Watts 2008), need to be explored further. We leave this for future work. If we take our present constraints at face value, we could possibly constrain nuclear reaction rates. Namely, Figure 8 shows that the $^{15}\text{O}(\alpha, \gamma)$ reaction rate cannot be a factor of 10 lower than the median rate of Davids et al. (2011)⁶.

If one adopts a particular dense matter equation of state, then our constraint can be used to determine M_{NS} . Alternatively, we could assume a stiff equation of state and use other astrophysical constraints for R_{NS} , or perhaps a photospheric radius expansion burst for the same bursting source, to determine M_{NS} . Either approach would provide additional data for the M_{NS} mass distribution, which is of interest for understanding the fates of massive stars.

7. CONCLUSIONS

To summarize, we assessed the influence of nuclear reaction rate variations on the results of multizone X-ray burst model calculations performed with the code MESA with respect to the influence of modified astrophysical conditions. Considering the 19 most influential reaction rate variations for the X-ray burst light curve identified by Cyburt et al. (2016) and using the astrophysical conditions that Meisel (2018) found best reproduce X-ray bursts from the GS 1826-24 years 1998, 2000, and 2007 bursting epochs, we assessed the impact of these rate variations on properties of the X-ray burst light curve and X-ray burst ashes.

We found that notable impacts on features of the X-ray burst light curve occur for the reaction rate variations $^{14}\text{O}(\alpha, p)/10$, $^{15}\text{O}(\alpha, \gamma)/10$, $^{18}\text{Ne}(\alpha, p) \times 30$, $^{22}\text{Mg}(\alpha, p)/10$, $^{24}\text{Mg}(\alpha, \gamma) \times 10$, $^{23}\text{Al}(p, \gamma)/30$, $^{59}\text{Cu}(p, \gamma)/100$, and $^{61}\text{Ga}(p, \gamma)/100$. However, none of the impacts are large enough to significantly change the conclusions about the accretion conditions for GS 1826-24 that were inferred by Meisel (2018).

We found that heating from electron-capture on the buried ashes in the neutron star crust is largely insen-

sitive to the nuclear reaction rate variations we investigated and was only significantly reduced for particularly helium-rich bursts. On the other hand, cooling from urca cycles involving buried ashes could be enhanced by the rate variations $^{15}\text{O}(\alpha, \gamma)/10$, $^{59}\text{Cu}(p, \gamma)/100$, and $^{61}\text{Ga}(p, \gamma)/100$. Using a heuristic for mapping between surface abundances and the inner crust impurity, we determined that $^{59}\text{Cu}(p, \alpha) \times 100$, $^{59}\text{Cu}(p, \gamma)/100$, and $^{61}\text{Ga}(p, \gamma)/100$ can likely influence $Q_{\text{imp}}^{\text{inner}}$ on a similar order as significant changes in accretion conditions; however, the overall changes are still modest.

Given the narrow range of astrophysical conditions that can reproduce the observed features of GS 1826-24, we were able to also determine constraints on the distance and surface gravitational redshift of this source, with the caveat that significant astrophysical uncertainties remain. Nonetheless, we demonstrate that reaction rate uncertainties are an additional obstacle to obtaining these constraints. Specifically, an influence on $d_{\text{b}}^{\zeta_{1/2}}$ and/or $1+z$ is observed for the rate variations $^{15}\text{O}(\alpha, \gamma)/10$, $^{14}\text{O}(\alpha, p)/10$, $^{18}\text{Ne}(\alpha, p) \times 30$, $^{23}\text{Al}(p, \gamma)/30$, $^{59}\text{Cu}(p, \gamma)/100$, and $^{61}\text{Ga}(p, \gamma)/100$. We identify $^{15}\text{O}(\alpha, \gamma)/10$ and $^{23}\text{Al}(p, \gamma)/30$ as particularly significant in this regard.

We stress that the reaction rates deemed influential may be different for other astrophysical conditions. As such, reaction rate sensitivity studies for a range of astrophysical conditions are welcome. Studies identifying the sets of astrophysical conditions that reproduce the light curve features observed for other X-ray bursting sources are also desired. Finally, it would be interesting to extend the present work to other nuclear physics uncertainties that have been shown to impact the X-ray burst light curve, e.g. nuclear masses (del Santo et al. 2014; Schatz & Ong 2017).

We thank the contributors to the MESA Marketplace (http://cococubed.asu.edu/mesa_market/) and the associated forum, who enabled the calculations presented here. This work was supported by the U.S. Department of Energy under grants DE-FG02-88ER40387 and de-sc0019042 and benefited from support by the National Science Foundation under grant PHY-1430152 (Joint Institute for Nuclear Astrophysics–Center for the Evolution of the Elements).

REFERENCES

- Almaraz-Calderon, S., Tan, W. P., Aprahamian, A., et al. 2012, *Phys. Rev. C*, 86, 065805
- Ayasli, S., & Joss, P. C. 1982, *Astrophys. J.*, 256, 637
- Bauswein, A., Just, O., Janka, H.-T., & Stergioulas, N. 2017, *Astrophys. J. Lett.*, 850, L34
- Bildsten, L. 2000, in *Proc. 10th Astrophys. Conf., AIP Conf. Ser.*, Vol. 522, 359
- Cavecchi, Y., Watts, A. L., & Galloway, D. K. 2017, *Astrophys. J.*, 851, 1
- Cumming, A., Macbeth, J., in’t Zand, J. J. M., & Page, D. 2006, *Astrophys. J.*, 646, 429
- Cyburt, R. H., Amthor, A. M., Heger, A., et al. 2016, *Astrophys. J.*, 830, 55
- Cyburt, R. H., et al. 2010, *Astrophys. J. Suppl. Ser.*, 189, 240, <http://reaclib.jinaweb.org>
- Davids, B., Cyburt, R. H., José, J., & Mythili, S. 2011, *Astrophys. J.*, 735, 40
- deBoer, R. J., Görres, J., Wiescher, M., et al. 2017, *Rev. Mod. Phys.*, 89, 035007
- Deibel, A., Cumming, A., Brown, E. F., & Page, D. 2015, *Astrophys. J. Lett.*, 809, L31
- Deibel, A., Meisel, Z., Schatz, H., Brown, E. F., & Cumming, A. 2016, *Astrophys. J.*, 831, 13
- del Santo, M., Meisel, Z., Bazin, D., et al. 2014, *Phys. Lett. B*, 738, 453
- Fattoyev, F. J., Piekarewicz, J., & Horowitz, C. J. 2018, *Phys. Rev. Lett.*, 120, 172702
- Fisker, J. L., Schatz, H., & Thielemann, F.-K. 2008, *Astrophys. J. Suppl. Ser.*, 174, 261
- Fisker, J. L., Thielemann, F.-K., & Wiescher, M. 2004, *Astrophys. J. Lett.*, 608, L61
- Fortune, H. T. 2012, *Phys. Rev. C*, 86, 068802
- Fujimoto, M. Y., Hanawa, T., & Miyaji, S. 1981, *Astrophys. J.*, 247, 267

⁶ This conclusion was reached by Meisel (2018) based on reproducing \mathcal{C} of the observed light curve.

- Galloway, D. K., Cumming, A., Kuulkers, E., et al. 2004, *Astrophys. J.*, 601, 466
- Galloway, D. K., Goodwin, A. J., & Keek, L. 2017, *Publ. Astron. Soc. Aust.*, 34, 19
- Galloway, D. K., Munro, M. P., Hartman, J. M., Dimitrios, P., & Chakrabarty, D. 2008, *Astrophys. J. Suppl. Ser.*, 179, 360
- Grevesse, N., & Sauval, A. J. 1998, *Space Sci. Rev.*, 85, 161
- Guillot, S., Servillat, M., Webb, N. A., & Rutledge, R. E. 2013, *Astrophys. J.*, 772, 7
- Gupta, S., Brown, E. F., Schatz, H., Möller, P., & Kratz, K.-L. 2007, *Astrophys. J.*, 662, 1188
- Heger, A., Cumming, A., Galloway, D. K., & Woosley, S. E. 2007, *Astrophys. J. Lett.*, 671, L141
- Heney, L., Vardya, M. S., & Bodenheimer, P. 1965, *Astrophys. J.*, 142, 841
- Hu, J., He, J. J., Parikh, A., et al. 2014, *Phys. Rev. C*, 90, 025803
- Iliadis, C., Longland, R., Champagne, A. E., Coc, A., & Fitzgerald, R. 2010, *Nucl. Phys. A*, 841, 31
- in't Zand, J. J. M., Visser, M. E. B., Galloway, D. K., et al. 2017, *Astron. & Astrophys.*, 606, A130
- Johnston, Z., Heger, A., & Galloway, D. K. 2018, *Monthly Notices of the Royal Astronomical Society*, sty757
- Joss, P. C. 1977, *Nature*, 270, 310
- Keek, L., & Heger, A. 2017, *Astrophys. J.*, 842, 113
- Koranda, S., Stergioulas, N., & Friedman, J. L. 1997, *Astrophys. J.*, 488, 799
- Lampe, N., Heger, A., & Galloway, D. K. 2016, *Astrophys. J.*, 819, 46
- Langer, C., Montes, F., Aprahamian, A., et al. 2014, *Phys. Rev. Lett.*, 113, 032502
- Lau, R., Beard, M., Gupta, S. S., et al. 2018, *Astrophys. J.*, 859, 62
- Matic, A., van den Berg, A. M., Haraheh, M. N., et al. 2009, *Phys. Rev. C*, 80, 055804
- Maurer, I., & Watts, A. L. 2008, *Mon. Not. R. Astron. Soc.*, 383, 387
- Meisel, Z. 2018, *Astrophys. J.*, 860, 147
- Meisel, Z., & Deibel, A. 2017, *Astrophys. J.*, 837, 13
- Meisel, Z., Deibel, A., Keek, L., Shternin, P., & Elfritz, J. 2018, *J. Phys. G*, 45, 093001
- Meisel, Z., et al. 2015, *Phys. Rev. Lett.*, 115, 162501
- Meisel, Z., George, S., Ahn, S., et al. 2016, *Phys. Rev. C*, 93, 035805
- Mohr, P., Longland, R., & Iliadis, C. 2014, *Phys. Rev. C*, 90, 065806
- Möller, P., Nix, J. R., Myers, W. D., & Swiatecki, W. J. 2018, *Atom. Nuc. Dat. Tab.*, 59, 185
- Parikh, A., José, J., Iliadis, C., Moreno, F., & Rauscher, T. 2009, *Phys. Rev. C*, 79, 045802
- Parikh, A., José, J., Moreno, F., & Iliadis, C. 2008, *Astrophys. J. Suppl. Ser.*, 178, 110
- Paxton, B., Bildsten, L., Dotter, A., et al. 2011, *Astrophys. J. Suppl. Ser.*, 192, 3, www.mesa.sourceforge.net
- Paxton, B., Cantiello, M., Arras, P., et al. 2013, *Astrophys. J. Suppl. Ser.*, 208, 4
- Paxton, B., Marchant, P., Schwab, J., et al. 2015, *Astrophys. J. Suppl. Ser.*, 220, 15
- Paxton, B., Schwab, J., Bauer, E. B., et al. 2018, *Astrophys. J. Suppl. Ser.*, 234, 34
- Press, W. H., Teukolsky, S. A., Vetterling, W. T., & Flannery, B. P. 1992, *Numerical Recipes in C: The Art of Scientific Computing*, 2nd edn. (Cambridge University Press)
- Reichert, J., Fehlmann, S., Cabezon, R., & Thielemann, F.-K. 2017, *JPS Conf. Proc.*, 14, 020509
- Schatz, H., Bildsten, L., Cumming, A., & Wiescher, M. 1999, *Astrophys. J.*, 524, 1014
- Schatz, H., Görres, J., Herndl, H., et al. 1997, *Phys. Rev. Lett.*, 79, 3845
- Schatz, H., & Ong, W.-J. 2017, *Astrophys. J.*, 844, 139
- Schatz, H., et al. 2014, *Nature*, 505, 62
- Shamsuzzoha Basunia, M. 2015, *Nucl. Dat. Sheets*, 127, 69
- Steiner, A. W., Heinke, C. O., Bogdanov, S., et al. 2018, *Mon. Not. R. Astron. Soc.*, 476, 421
- Turlione, A., Aguilera, D. N., & Pons, J. A. 2015, *Astron. & Astrophys.*, 577, A5
- van Wormer, L., Görres, J., Iliadis, C., Wiescher, M., & Thielemann, F.-K. 1994, *Astrophys. J.*, 432, 326
- Wallace, R. K., & Woosley, S. E. 1981, *Astrophys. J. Suppl. Ser.*, 45, 389
- Weaver, T. A., Zimmerman, G. B., & Woosley, S. E. 1978, *Astrophys. J.*, 225, 1021
- Weinberg, N., Bildsten, L., & Schatz, H. 2006, *Astrophys. J.*, 639, 1018
- Wiescher, M., Görres, J., & Schatz, H. 1999, *J. Phys. G.*, 25, R133
- Woosley, S. E., Heger, A., Cumming, A., et al. 2004, *Astrophys. J. Suppl. Ser.*, 151, 75
- Zamfir, M., Cumming, A., & Galloway, D. K. 2012, *Astrophys. J.*, 749, 69